Prediction of a BeP_2 monolayer with a compression-induced Dirac semimetal state

Xiaoyin Li and Qian Wang*

Center for Applied Physics and Technology, Department of Materials Science and Engineering, College of Engineering, Peking University, Beijing 100871, China;

Key Laboratory of High Energy Density Physics Simulation, Ministry of Education, Beijing 100871, China;

and Collaborative Innovation Center of IFSA (CICIFSA), Shanghai Jiao Tong University, Shanghai 200240, China

(Received 25 August 2017; revised manuscript received 9 January 2018; published 13 February 2018)

We have identified a two-dimensional (2D) beryllium diphosphide (BeP_2) structure using a global structure search combined with first-principles calculations. Phonon calculations and molecular dynamics simulation confirm that the structure is dynamically and thermally stable. Electronic structure calculations show that the 2D sheet is a direct band gap semiconductor with a small band gap of 0.15 eV, and the intrinsic acoustic-phonon-limited carrier mobility of the structure can reach $\sim 10^4$ $cm^2V^{-1}s^{-1}$ for both electrons and holes with anisotropic features in the x and y directions. More interestingly, both mechanical and chemical compression can close the band gap and the structure turns to a Dirac semimetal with the Dirac cones located exactly at the Fermi level. The emerged Dirac semimetal state is direction dependent, with a linear band dispersion in the x direction and a quadratic one in the y direction. Moreover, it is demonstrated that the Dirac point is symmetry protected in the absence of spin-orbit coupling (SOC). In BeP_2, the SOC is too weak to alter the semimetal feature except for the cases at extremely low temperatures. The band gap closing mechanism is further clarified by using the tight-binding (TB) method.

DOI: 10.1103/PhysRevB.97.085418

I. INTRODUCTION

The discovery of graphene [1] opened the door to exploring two-dimensional (2D) materials with new physics and potential applications [2,3]. Besides the distinctive chemical and mechanical properties, graphene also possesses exceptional carrier mobility [4], massless Dirac fermions [5], and the quantum Hall effect [6], which originate from its unique Dirac cone structure. These findings motivated people to search for other 2D materials with Dirac cones including some carbon allotropes (e.g., graphynes [7,8], phagraphene [9]), silicene [10,11], germanene [12], and some boron allotropes [13–15]. Moreover, recently it was found experimentally and theoretically that a Dirac semimetal state can be induced by doping potassium (K) on the surface of few-layer black phosphorus (P) [16,17]. At the critical dopant density, the electronic state is tuned from a moderate-gap semiconductor to an anisotropic Dirac semimetal, with a linear dispersion in the armchair direction but a quadratic dispersion in the zigzag direction. The discovery of metal-doping induced Dirac state in few-layer black phosphorus [16,17] is inspiring, thus a question has been raised: Is it possible to realize the Dirac semimetal state in a phosphorus-metal alloyed sheet?

Here we focus on a P-Be alloyed sheet because Be has been widely used as one of the constituent elements in 2D binary compounds, including h-BeS [18], Be_2C [19], and Be_5C_2 [20], to name a few. Moreover, an N-Be sheet is found to be stable with exceptional properties [21]. Since N and P are in the same group in the periodic table of the elements, it is natural to explore whether the P-Be binary compound can be stabilized in a 2D form, and, if so, does it possess unusual Dirac semimetal state? In this study, by means of a structural prediction method and first-principles calculations, we predict a previously unreported BeP_2 sheet, which possesses robust structural stability, high and anisotropic carrier mobility, as well as exotic electronic properties. Especially, both equi-biaxial compressive strain and B and C codoping can tune the sheet to be a Dirac semimetal with Dirac cones exactly located at the Fermi level. The emerged Dirac point is protected by symmetry in the absence of SOC. However, the SOC in the modulated BeP_2 structure is very weak, thus it will not alter the semimetal feature of the structure. The underlying mechanism of band closing is analyzed as well through the tight-binding (TB) method.

II. COMPUTATIONAL METHODS

The structure search is performed by using a particle-swarm optimization (PSO) based global structural search method implemented in the Crystal structure AnaLYsis by Particle Swarm Optimization (CALYPSO) code [22]. First-principles calculations within the framework of density functional theory (DFT) are performed using the Vienna Ab initio Simulation Package (VASP) [23]. The projector augmented wave (PAW) [24] pseudopotential is employed with a kinetic energy cutoff of 350 eV. In most calculations, the Perdew-Burke-Ernzerhof (PBE) [25] functional is used to treat the exchange-correlation interactions while the Heyd-Scuseria-Ernzerhof (HSE06) [26,27] functional is used to achieve more accurate electronic band gaps. The Brillouin zone is sampled by the k-point meshed following the Monkhorst-Pack scheme [28], with a grid density of $2\pi \times 0.02$ $Å^{-1}$. Lattice constants and atomic positions are fully optimized by using the conjugated gradient algorithm without any symmetry related constraints,

*qianwang2@pku.edu.cn

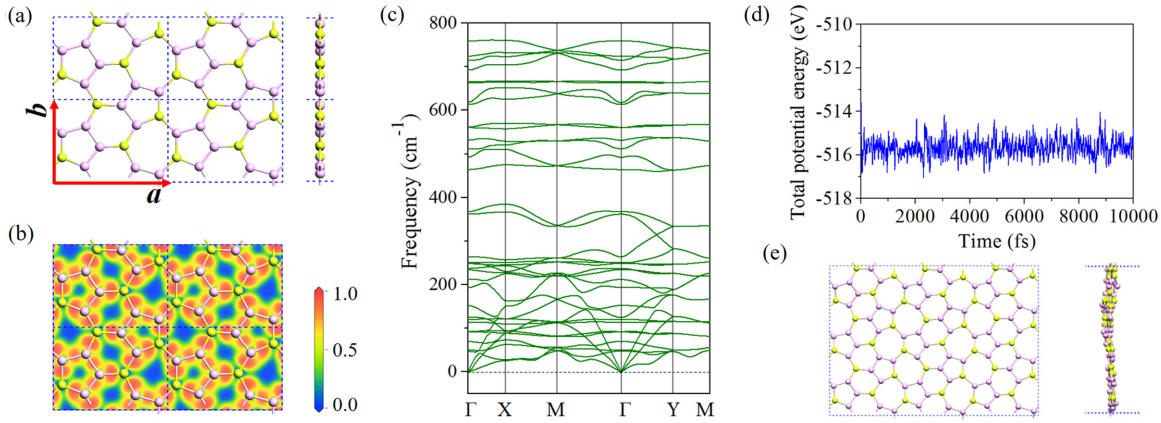

FIG. 1. (a) Top and side views of BeP_2 structure. The blue dashed rectangle represents the unit cell of the structure, and red arrows represent the lattice axes. (b) Slice form (crossing the monoatomic thick structure) of electron localization function of BeP_2. (c) Phonon spectra of BeP_2. The high symmetric paths in the first Brillouin zone are Γ (0,0) – X (1/2,0) – M (1/2,1/2) – Γ (0,0) – Y (0,1/2) – M (1/2,1/2). (d) Fluctuation of total potential energy of the BeP_2 sheet during the AIMD simulation at 300 K. (e) Structure snapshots of the BeP_2 sheet at the end of the simulation.

and the energy and force convergence criteria are set to be 10^{-5} eV and 10^{-3} eV/Å, respectively. Phonon dispersion is calculated based on density functional perturbation theory with the linear response as implemented in the QUANTUM ESPRESSO package [29]. The TB matrix elements are calculated by projecting Bloch states onto maximally localized Wannier functions (MLWFs), using the WANNIER90 package [30] interfaced with QUANTUM ESPRESSO [29]. The edge energy spectrum is calculated based on the iterative Greens function method [31], which is implemented in the WANNIER tools package [32].

III. RESULTS AND DISCUSSION

A. Structure and stability

The most stable structure of BeP_2 obtained from the global structure search is presented in Fig. 1(a); it is a planar and atomic thick sheet consisting of pentagons, hexagons, and heptagons as the structural motifs. The lattice of BeP_2 is rectangular, with associated lattice constants of $a = 9.70$ Å and $b = 6.98$ Å. Each unit cell contains four Be atoms and eight P atoms. The plane symmetry of BeP_2 is Pg (plane group no. 4); accordingly, there are two (four) inequivalent Be (P) atoms in one unit cell. In this structure, Be atoms are trigonally bonded to three adjacent P atoms, while P atoms are trigonally bonded to two Be atoms and one P atom or one Be atom and two P atoms. Here four P atoms in BeP_2 can be viewed as a P_4 chain. These P_4 chains are connected together through Be atoms as linkers to form the 2D sheet. Due to the electronegativity difference between Be and P, charge transfer from Be atoms to the P_4 chains is expected and confirmed by calculating the electron localization function (ELF). The value of ELF is renormalized to between 0.0 and 1.0. The values 0.5 and 1.0 represent the fully delocalized and fully localized electrons, respectively, while the value 0.0 refers to a very low charge density. From the result in Fig. 1(b), the electrons are localized around the P_4 units, while the charge density around the Be atoms is low, which means that the P_4 units are electron abundant while the Be atoms are electron deficient. To quantify the charge transfer we perform Bader charge analysis [33]. The results show that each Be atom donates ∼1.5 electrons and consequently each P_4 unit receives ∼3 electrons, which distribute around the P sites, as shown in Fig. 1(b).

Before studying the properties of BeP_2, we carefully examine its structural stability. We first calculate the cohesive energy of BeP_2, which is defined as $E_c = -[E(BeP_2) - E(Be) - 2E(P)]/3$, to explore its energetic stability and experimental accessibility. The calculated cohesive energy of BeP_2 is 3.53 eV/atom, comparable to experimentally synthesized silicene (3.97 eV/atom) and phosphorene (3.48 eV/atom), confirming the thermodynamic stability of the structure and implying the possibility of realizing such a 2D sheet experimentally. Then we calculate the phonon dispersion of BeP_2 with results shown in Fig. 1(c). From the phonon spectra, one can see that there is no imaginary mode in the entire Brillouin zone, indicating that the BeP_2 sheet is dynamically stable. We also examine the thermal stability of the structure by performing *ab initio* molecular dynamics (AIMD) simulation. A (3×3) supercell containing 108 atoms is constructed to perform the simulation. As shown in Figs. 1(d) and 1(e), after heating at 300 K for 10 picoseconds (ps), the structure retains its integrity without appreciable distortion, and the total potential energy only fluctuates around a constant value, suggesting that the 2D sheet is thermally stable at room temperature.

Since the lattice is fixed during the AIMD simulation, we calculate the elastic constants to examine mechanical stability of the structure under small lattice distortion. Using the finite distortion approach, we obtain the elastic constants $C_{11} = 68$ N/m, $C_{22} = 72$ N/m, $C_{12} = 31$ N/m, and $C_{66} = 25$ N/m, which satisfy the Born-Huang criteria of $C_{11} > |C_{12}| > 0$ and $C_{66} > 0$ for mechanical stability. The in-plane Young's modulus of BeP_2 along the x (E_a) and y (E_b) directions, which can be derived from the elastic constants by equations of $E_a = \frac{C_{11}^2 - C_{12}^2}{C_{11}}$ and $E_b = \frac{C_{22}^2 - C_{12}^2}{C_{22}}$, are calculated to be 54 and 59 N/m, respectively. The Young's moduli of BeP_2 are less than those of graphene ($E_a = E_b = 342$ N/m) [34], but comparable to those of silicene ($E_a = E_b = 62$ N/m) [35], implying a good in-plane stiffness of the 2D sheet.

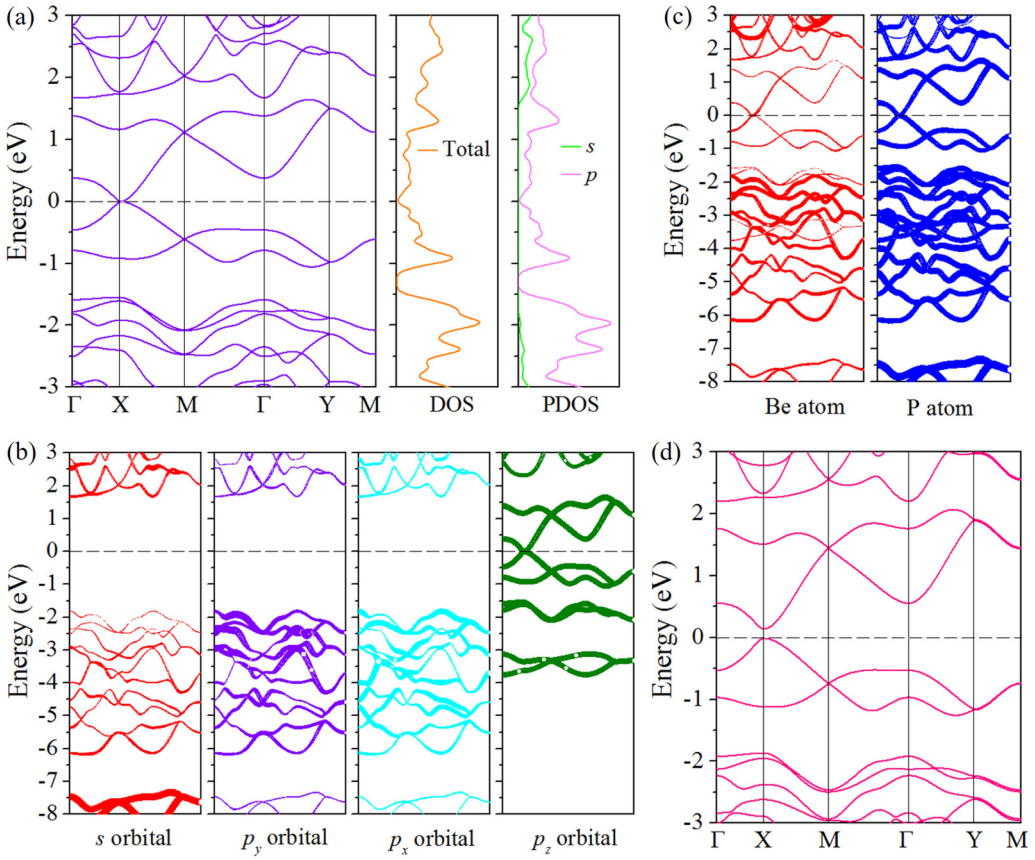

FIG. 2. (a) Electronic band structure, total DOS, and PDOS of BeP_2 calculated by using the PBE functional. (b) and (c) Orbital-decomposed and atom-decomposed band structures of BeP_2 at the PBE level. (d) Electronic band structure of BeP_2 calculated by using the HSE06 functional.

B. Electronic and transport properties

To explore the electronic properties of the BeP_2 monolayer, we calculate its electronic band structures. As shown in Fig. 2(a), the calculated results at the PBE level indicate that BeP_2 is a semimetal with zero density of states (DOS) at the Fermi energy. The orbital projected DOS (PDOS) shows that the bands near the Fermi level mainly originate from the p orbitals. To get more details on the orbital composition of the energy bands, we calculate the orbital- and atom-decomposed band structures of the BeP_2 sheet. The results plotted in Figs. 2(b) and 2(c) show that near the Fermi energy there are eight energy bands entirely decoupled from the others, which are mainly from the eight P-p_z orbitals.

Because of the well-known underestimation of the PBE functional on predicting band gap size of semiconductors, and a semiconductor with a small band gap might be falsely concluded to be a metal, we use the hybrid HSE06 functional to get more accurate band structures. The results are presented in Fig. 2(d); they show that BeP_2 is a direct band gap semiconductor with the valence band maximum (VBM) and the conduction band minimum (CBM) both located at the X point, and it has a narrow band gap of 0.15 eV. Moreover, the bands near the VBM and CBM exhibit notable in-plane dispersion behavior, indicating that the BeP_2 sheet may have relatively high carrier mobility.

Since the transport properties of a material are governed to a large extent by its carrier mobilities, we next study the carrier mobilities of the BeP_2 monolayer in both x and y directions. At room temperature, the coherent wavelength of thermally activated electrons or holes is close to the acoustic phonon wavelength and much larger than the lattice constants, in which situation the deformation potential (DP) theory proposed by Bardeen and Shockley [36] can be applied. This phonon-limited scattering model has been successfully employed to study the charge transport properties of many 2D semiconductors [37–40]. The acoustic-phonon-limited carrier mobility in the BeP_2 sheet can be obtained by using the following expression [41]:

$$\mu_x = \frac{e\hbar^3\left(\frac{5C_{11}+3C_{22}}{8}\right)}{k_B T (m_x^*)^{\frac{3}{2}}(m_y^*)^{\frac{1}{2}}\left(\frac{9E_{1x}^2+7E_{1x}E_{1y}+4E_{1y}^2}{20}\right)} \quad (1)$$

which includes the anisotropic characteristics of effective mass, elastic modulus, as well as deformation potential. Here C is the elastic modulus, T is temperature that is taken to be 300 K in our calculations, m^* and E_1 represent the effective mass and DP constant in the transport direction, and k_B and $\hbar$ are Boltzmann and reduced Planck constants, respectively. The DP constant is defined as the energy shift of band edge with respect to the lattice dilation and compression along the transport direction. All the calculated results are summarized in Table I. It shows that the BeP_2 sheet exhibits a relatively high carrier mobility $\sim 10^4$ $cm^2V^{-1}s^{-1}$ for both electrons and holes, notably higher than that of phosphorene, MoS_2, and

TABLE I. Deformation potential constant E_1, elastic modulus C, effective mass m^*, and mobility μ for electrons and holes along x and y directions in BeP_2 at 300 K.

Carrier type	Direction	E_1 (eV)	C (N/m)	$m^*(m_e)$	μ ($\times 10^3$ cm^{2}V^{-1}s^{-1})
Electron	x	1.730	68	0.074	68.27
	y	1.048	72	0.241	27.09
Hole	x	1.446	68	0.073	75.16
	y	0.584	72	0.514	14.35

TiS_3 monolayers [37–39], indicating its potential applications in nanoelectronics. Moreover, the carrier mobility along the x direction is much higher than that along the y direction, showing remarkable anisotropic characteristics.

C. Strain-induced Dirac semimetal state

The investigation of influences of external perturbations such as strain, doping, pressure, and temperature on semiconductor properties has triggered intensive research activities for decades [42–51]. Tailoring electronic properties of semiconducting materials is critical for their applications in nanoelectronic devices. Moreover, a lot of recent works have demonstrated the sensitive dependence of energy gaps of semiconductors on external strain [52–54], pressure [55], electric fields [56], and chemical doping [16,17]. In this study, the band gap size of BeP_2 is only 0.15 eV, thus tractable for tuning to achieve band gap closure. After applying equi-biaxial strain and compressing the lattice constants by 4%, the BeP_2 sheet transforms from a direct band gap semiconductor to a Dirac semimetal with the Dirac cone located exactly on the Fermi energy. For the sake of convenience of discussion, we term the structure under 4% compressive strain as c-BeP_2. The calculated band structures of c-BeP_2 in Fig. 3 show that the valence band and conduction band are inverted at the X point, and the two bands cross with each other at two k points, which are marked as $\pm K_D(1/2,\pm k_y)$ in the figure. From the three-dimensional (3D) band structures shown in Fig. 3(a), the bands in the vicinity of the Dirac point exhibit linear dispersion in both x and y directions, leading to zero electron effective mass, as in graphene. Moreover, the band structures in Fig. 3(b) show that the valence band and conduction band are linear along the x direction but quadratic along the y direction, similar to that of semimetallic K-doped few-layer black phosphorus [16,17]. The isoenergetic contours in Fig. 3(c) further demonstrate the existence of Dirac points in c-BeP_2. It shows that as the energy increases from the valence band to the Fermi level, the elliptical contour shrinks and disconnects, becoming two separate circles, and the two circles shrink further to two Dirac points located exactly on the Fermi surface. A similar transition also happens as the energy level is lowered from the conduction band to the Fermi energy. Here the emerged Dirac points are accidental degeneracies of the energy bands induced by band inversion. After the inversion of the valence and conduction bands, the crossing points in c-BeP_2 become stable Dirac points protected by the glide reflection symmetry and time reversal symmetry of the lattice as stated in the generalized von Neumann-Wigner theorem [57], where the number of constraints on the lattice necessary to have band contacts is clearly given. Breaking the symmetry opens up a gap at the Dirac point (see details in the Supplemental Material [58]).

We then examine the band structures of c-BeP_2 with SOC taken into account. The HSE06 result is presented in Fig. 3(d). It shows that a small band gap of 1 meV is opened up in the presence of SOC. The band gap opening can be clarified by symmetry analysis. For the k points on the X-M line, the symmetry group is C_{2v}. In the absence of SOC, the conduction band (CB) and valence band (VB) along the X-M line belong to different irreducible representations (A_2 and B_2 respectively), which prohibits hybridization between them, resulting in the unavoidable band crossing. While in the presence of SOC, the double point group of C_{2v} should be considered. Because it only has one irreducible representation Γ_5, the CB and VB

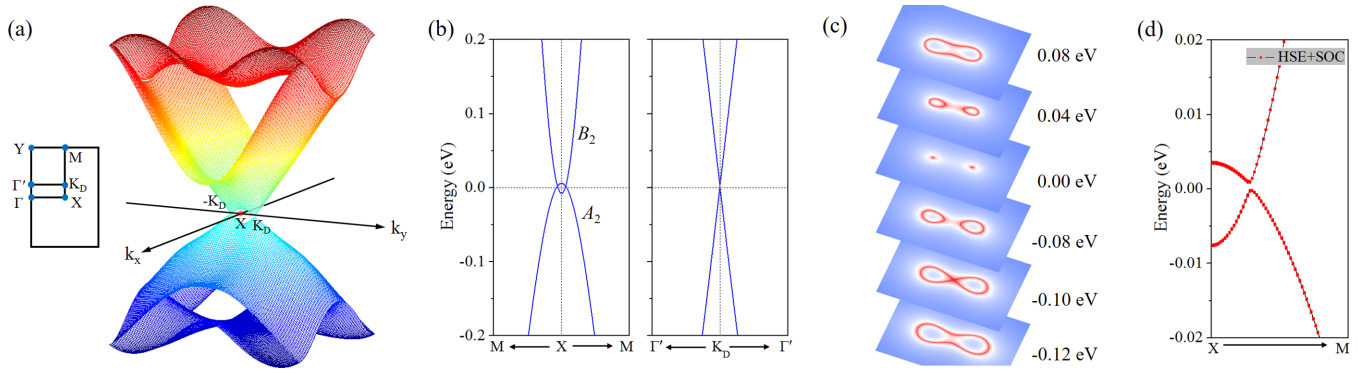

FIG. 3. Electronic band structures of c-BeP_2 calculated based on the HSE06 functional. (a) 3D (k_x, k_y, energy) band structure of c-BeP_2. The axes are located at the Fermi energy. (b) Band structures of c-BeP_2 along the y (left plane) and the x (right plane) directions, respectively. (c) Constant energy contours of c-BeP_2 at different energy levels. (d) Band structure of c-BeP_2 with SOC.

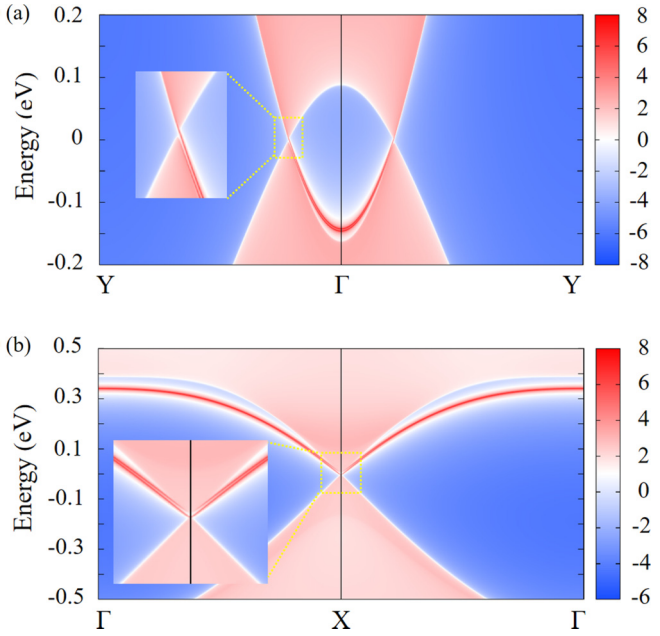

FIG. 4. Edge density of states of c-BeP_2 with edge terminated in (a) the x direction and (b) the y direction. Low, medium, and high density of states are indicated by blue, white and red colors, respectively.

both belong to the same irreducible representation, and they can interact with each other, resulting in the band gap opening. To determine the topological nature of c-BeP_2, we calculate its Z_2 invariant since time reversal symmetry is preserved in the structure. The calculated result of $Z_2 = 1$ indicates the nontrivial band topology of c-BeP_2. Therefore, c-BeP_2 is nominally a 2D topological insulator. However, considering that the SOC in c-BeP_2 is negligibly weak, we can treat it as a semimetal phase in almost all cases except those at extremely low temperatures.

It is known that one of exotic features of topological materials is the robust surface states or edge states. Here, for the c-BeP_2 sheet, we calculate its edge states by cutting the sheet into one-dimensional (1D) nanoribbons. By individually terminating the sheet in the x and y directions, we get edge states for the two directions respectively. The results presented in Fig. 4 show that the edge states both have gapless features regardless of their terminating directions, in good agreement with the results from topological invariant calculation.

D. Tight-binding model for the BeP_2 Monolayer

From the above analysis of the orbital composition of the energy bands near the Fermi level, we note that there are eight bands entirely decoupled from the others and primarily originating from the P-p_z orbitals. Therefore, it is possible and reasonable to model these bands using a TB Hamiltonian of P-p_z orbitals:

$$H = U \sum_i c_i^\dagger c_i + \sum_{ij} (t_{ij} c_i^\dagger c_j + \text{H.c.}). \quad (2)$$

Here $c_i^\dagger$ and c_i represent the creation and annihilation operators of an electron in the ith P-p_z orbital, U is the onsite energy, and

TABLE II. Hopping integral parameters for BeP_2 and c-BeP_2.

	BeP_2	c-BeP_2
$t_1 \sim t_3$	−1.54	−1.60
$t_4 \sim t_9$	−0.41	−0.52
t_{10}	0.13	0.15
$t_{11} \sim t_{15}$	0.11	0.12

t_{ij} is the hopping integral parameter between the ith and jth orbitals. The orbitals in our TB model are all P-p_z orbitals, thus we can simply set the onsite energy to be 0 eV for all the sites. We consider the largest 15 hopping pairs (see details in the Supplemental Material [58]) and the hopping integral parameters are determined by fitting the DFT band structures, which are summarized in Table II. By diagonalizing the simplified TB model Hamiltonian, we obtain the electronic bands of BeP_2, as shown in Fig. 5(a), which reproduce well the band alignment and dispersion features of the DFT band structures.

By using the constructed TB model, we can explain the mechanism of band gap closing in BeP_2 under compressive strain. For comparison, we derive the hopping integral parameters of c-BeP_2 as well and the results are listed in Table II. With these parameters and TB model Hamiltonian, the derived bands of c-BeP_2 are presented in Fig. 5(b), and are in good agreement with the results of DFT calculations. We notice that the hopping parameter of c-BeP_2 is larger than the corresponding result of BeP_2 in absolute value. It is consistent with the external perturbation that was applied to the structure to tune the semiconductor to be a semimetal. This can be understood as the following: the applied compressive strain decreases the distance between atoms, thus increases the overlap of wave functions, and the hopping between different orbitals becomes easier; the easier hopping corresponds to larger hopping integral, and the larger hopping integral leads to the inversion of valence and conduction band at the X point as well as the occurrence of bands crossing on the X-M path. This picture provides the underlying mechanism why the compressive strain can induce the transition from a semiconductor to a Dirac semimetal.

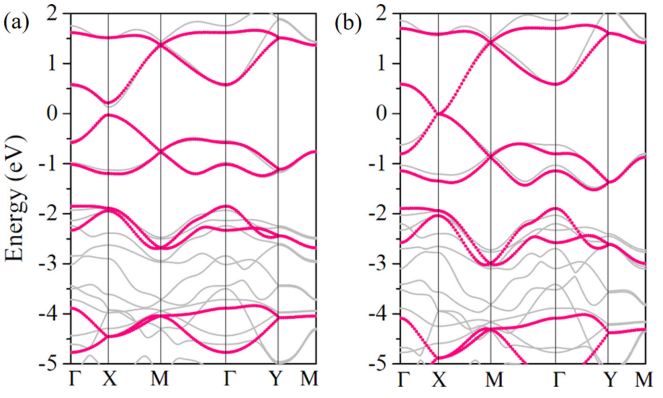

FIG. 5. Band structures of (a) BeP_2 and (b) c-BeP_2 respectively. The red dot lines represent the results derived from the TB model and the gray solid lines are the results of first-principles calculations.

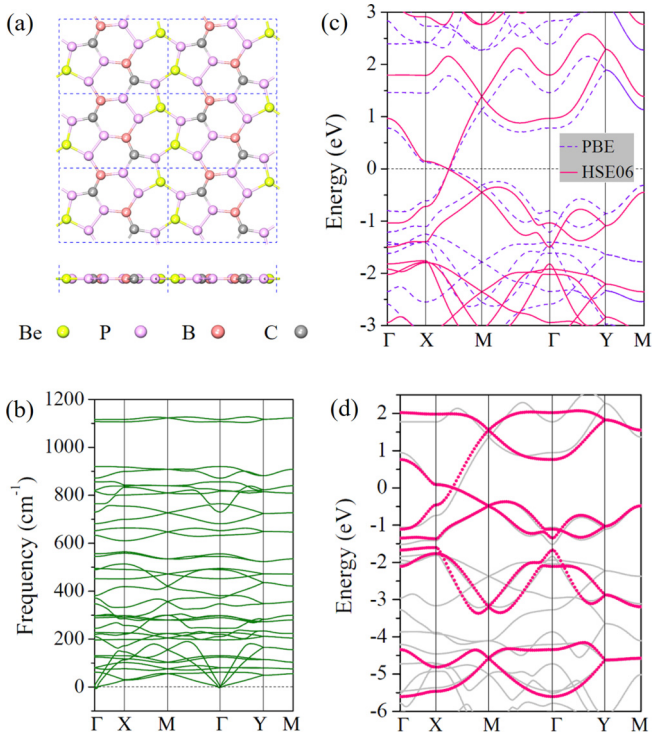

FIG. 6. (a) Optimized geometrical structure, (b) phonon spectra, (c) electronic band structure, and (d) TB model derived bands of the B and C co-doped BeP_2 structure. In panel (d), the red dotted lines represent the results from the TB model and the gray solid lines are the first-principles results.

E. Feasibility of Dirac point in BeP_2

Finally, to assess the feasibility of Dirac point in BeP_2, we calculate the phonon dispersion of the compressed structure. The phonon dispersion of c-BeP_2 in Fig. S4(b) [58] shows that there are negative frequencies in the Brillouin zone, indicating the existence of an energetically favorable deformation in the planar sheet. Further analysis shows that the vibration directions of these negative frequencies are all perpendicular to the structure plane, just like those in compressed graphene [59]. Since both experimental and theoretical results show that compressive strain will induce corrugations or ripples in graphene [60,61], we introduce a cosine-like perturbation on a rectangular 2×1 supercell of BeP_2 under 4% biaxial compressive strain. The optimized structure and calculated phonon dispersion are shown in Figs. S4(c) and S4(d). One can see that the cosine-like buckling erases almost all negative phonon modes, similar to that in the compressed graphene [59].

The above results indicate that 4% compressive strain may induce buckling in the suspended BeP_2 sheet. To avoid such a problem, we consider chemical compression [62] rather than mechanical compression. Based on electronic structure calculations and TB model analysis of c-BeP_2, we deduce that if we dope the BeP_2 structure with elements that have smaller atomic size while keeping the pristine electron filling, we might obtain the inverted band with Dirac points as well. Here we choose B and C to co-dope the BeP_2 sheet in order to satisfy the electron-counting requirement, and get the optimized structure as shown in Fig. 6(a). The lattice parameters of the co-doped structure change to $a = 8.99$ Å, $b = 6.17$ Å from $a = 9.31$ Å, $b = 6.70$ Å of c-BeP_2. The phonon calculation results in Fig. 6(b) confirm the dynamical stability of the co-doped BeP_2 structure. More importantly, the band inversion at the Fermi level is induced [see Fig. 6(c)], and the 3D band structure in Fig. 7(a) shows the existence of Dirac cones at the Fermi level. We also calculate the band structure of the co-doped BeP_2 sheet when SOC is taken into account. Similar to the situation in c-BeP_2, a band gap is opened up at the Dirac point, calculated to be 0.2 (1.4) meV at the PBE (HSE06) level, which is very small and not expected to alter the semimetal phase of the co-doped BeP_2 structure except at extremely low temperatures. The calculated Z_2=1 and gapless edge states [see Figs. 7(b) and 7(c)] both demonstrate the topological nontrivial nature of the co-doped BeP_2 sheet, indicating that the Dirac point in BeP_2 is achievable via chemical compression, namely, B and C co-doping.

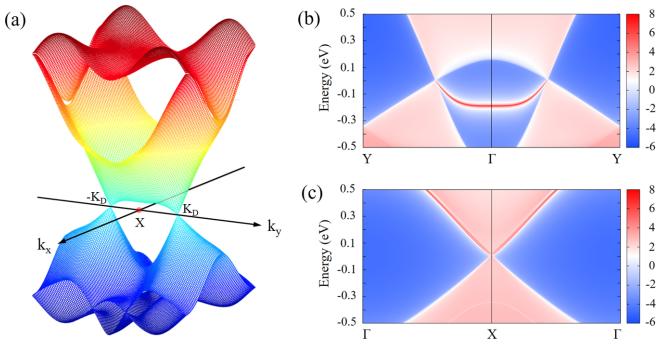

FIG. 7. (a) 3D (k_x, k_y, energy) band structure of the co-doped BeP_2 sheet. The axes are located at the Fermi energy. (b) and (c) are edge density of states of the co-doped BeP_2 structure with edge terminated in the x and y directions respectively.

We construct a TB model Hamiltonian of the co-doped BeP_2 structure as well using the C-p_z and P-p_z orbitals. By fitting the first-principles band structure at the HSE06 level, we get the corresponding onsite energies and hopping integral parameters, as summarized in Table III. Due to the B and C co-doping, the eight orbitals have different onsite energies. With these parameters and the TB model Hamiltonian, we derive the bands in Fig. 6(d), which are in good agreement with the first-principles results. More importantly, the hopping

TABLE III. Onsite energies U and hopping integral parameters t (eV) of the B and C co-doped BeP_2 structure.

Onsite energy	U_1	U_2	U_3	U_4	U_5	U_6	U_7	U_8		
	−0.6	−0.6	0	0	0	0	0.7	0.7		
Hopping integral	t_1, t_2	t_3	t_4	t_5, t_9	t_6	t_7, t_8	t_{10}, t_{11}	t_{12}	t_{13}, t_{15}	t_{14}
	−1.67	−1.46	−0.97	−0.41	−0.44	−0.75	0.26	0.12	0.20	0.16

integral parameters here are all larger than the corresponding results of pristine BeP_2 in absolute value, which agrees well with our conclusion that the larger hopping integral leads to the band inversion at the X point (see Sec. III D).

IV. CONCLUSIONS

In summary, through first-principles calculations combined with crystal structure prediction methods, we have proposed a novel 2D BeP_2 structure, which is confirmed to be stable dynamically and thermally. The structure is a direct band gap semiconductor at the HSE06 level. Based on the deformation potential theory, the acoustic-phonon-limited carrier mobility in BeP_2 reaches $\sim 10^4$ $cm^2V^{-1}s^{-1}$, which is even higher than that of widely studied phosphorene, MoS_2, and TiS_3 monolayers. By mechanical or chemical compression, the VBM and CBM at the X point are inverted, and the BeP_2 monolayer becomes a Dirac semimetal. The band inversion mechanism is clarified using the TB model constructed based on the P-p_z orbitals. The high carrier mobility and novel strain tunable Dirac semimetal state in the BeP_2 sheet make it a promising 2D material with potential device applications.

ACKNOWLEDGMENTS

This work is partially supported by grants from the National Natural Science Foundation of China (Grants No. NSFC-51471004 and No. NSFC-21773004) and the National Key Research and Development Program of China (Grants No. 2016YFE0127300 and No. 2017YFA0205003). The calculations were carried out at the High Performance Computing Platform of CAPT at Peking University, China.

[1] K. S. Novoselov, A. K. Geim, S. V. Morozov, D. Jiang, Y. Zhang, S. V. Dubonos, I. V. Grigorieva, and A. A. Firsov, Science **306**, 666 (2004).
[2] D. S. L. Abergel, V. Apalkov, J. Berashevich, K. Ziegler, and T. Chakraborty, Adv. Phys. **59**, 261 (2010).
[3] K. S. Novoselov, V. I. Falko, L. Colombo, P. R. Gellert, M. G. Schwab, and K. Kim, Nature (London) **490**, 192 (2012).
[4] K. I. Bolotin, K. J. Sikes, Z. Jiang, M. Klima, G. Fudenberg, J. Hone, P. Kim, and H. L. Stormer, Solid State Commun. **146**, 351 (2008).
[5] K. S. Novoselov, A. K. Geim, S. V. Morozov, D. Jiang, M. I. Katsnelson, I. V. Grigorieva, S. V. Dubonos, and A. A. Firsov, Nature (London) **438**, 197 (2005).
[6] Y. Zhang, Y.-W. Tan, H. L. Stormer, and P. Kim, Nature **438**, 201 (2005).
[7] D. Malko, C. Neiss, F. Viñes, and A. Görling, Phys. Rev. Lett. **108**, 086804 (2012).
[8] H. Huaqing, D. Wenhui, and L. Zhirong, New J. Phys. **15**, 023004 (2013).
[9] Z. Wang, X.-F. Zhou, X. Zhang, Q. Zhu, H. Dong, M. Zhao, and A. R. Oganov, Nano Lett. **15**, 6182 (2015).
[10] P. Vogt, P. De Padova, C. Quaresima, J. Avila, E. Frantzeskakis, M. C. Asensio, A. Resta, B. Ealet, and G. Le Lay, Phys. Rev. Lett. **108**, 155501 (2012).
[11] A. Fleurence, R. Friedlein, T. Ozaki, H. Kawai, Y. Wang, and Y. Yamada-Takamura, Phys. Rev. Lett. **108**, 245501 (2012).
[12] S. Cahangirov, M. Topsakal, E. Aktürk, H. Sahin, and S. Ciraci, Phys. Rev. Lett. **102**, 236804 (2009).
[13] X.-F. Zhou, X. Dong, A. R. Oganov, Q. Zhu, Y. Tian, and H.-T. Wang, Phys. Rev. Lett. **112**, 085502 (2014).
[14] H. Zhang, Y. Xie, Z. Zhang, C. Zhong, Y. Li, Z. Chen, and Y. Chen, J. Phys. Chem. Lett. **8**, 1707 (2017).
[15] W.-c. Yi, W. Liu, J. Botana, L. Zhao, Z. Liu, J.-y. Liu, and M.-s. Miao, J. Phys. Chem. Lett. **8**, 2647 (2017).
[16] J. Kim, S. S. Baik, S. H. Ryu, Y. Sohn, S. Park, B.-G. Park, J. Denlinger, Y. Yi, H. J. Choi, and K. S. Kim, Science **349**, 723 (2015).
[17] S. S. Baik, K. S. Kim, Y. Yi, and H. J. Choi, Nano Lett. **15**, 7788 (2015).
[18] J. Yu and W. Guo, J. Phys. Chem. Lett. **4**, 1856 (2013).
[19] Y. Li, Y. Liao, and Z. Chen, Angew. Chem. Int. Ed. **53**, 7248 (2014).
[20] Y. Wang, F. Li, Y. Li, and Z. Chen, Nat. Commun. **7**, 11488 (2016).
[21] C. Zhang and Q. Sun, J. Phys. Chem. Lett. **7**, 2664 (2016).
[22] Y. Wang, J. Lv, L. Zhu, and Y. Ma, Comput. Phys. Commun. **183**, 2063 (2012).
[23] G. Kresse and J. Furthmuller, Phys. Rev. B **54**, 11169 (1996).
[24] P. E. Blöchl, Phys. Rev. B **50**, 17953 (1994).
[25] J. P. Perdew, K. Burke, and M. Ernzerhof, Phys. Rev. Lett. **77**, 3865 (1996).
[26] J. Heyd, G. E. Scuseria, and M. Ernzerhof, J. Chem. Phys. **118**, 8207 (2003).
[27] J. Heyd, G. E. Scuseria, and M. Ernzerhof, J. Chem. Phys. **124**, 219906 (2006).
[28] H. J. Monkhorst and J. D. Pack, Phys. Rev. B **13**, 5188 (1976).
[29] G. Paolo, B. Stefano, B. Nicola, C. Matteo, C. Roberto, C. Carlo, C. Davide, L. C. Guido, C. Matteo, D. Ismaila, C. Andrea Dal, G. Stefano de, F. Stefano, F. Guido, G. Ralph, G. Uwe, G. Christos, K. Anton, L. Michele, M.-S. Layla, M. Nicola, M. Francesco, M. Riccardo, P. Stefano, P. Alfredo, P. Lorenzo, S. Carlo, S. Sandro, S. Gabriele, P. S. Ari, S. Alexander, U. Paolo, and M. W. Renata, J. Phys.: Condens. Matter **21**, 395502 (2009).
[30] A. A. Mostofi, J. R. Yates, Y.-S. Lee, I. Souza, D. Vanderbilt, and N. Marzari, Comput. Phys. Commun. **178**, 685 (2008).
[31] M. P. L. Sancho, J. M. L. Sancho, J. M. L. Sancho, and J. Rubio, J. Phys. F: Met. Phys. **15**, 851 (1985).
[32] Q. Wu and S. Zhang, https://github.com/quanshengwu/wannier_tools (2017).
[33] E. Sanville, S. D. Kenny, R. Smith, and G. Henkelman, J. Comput. Chem. **28**, 899 (2007).
[34] R. C. Andrew, R. E. Mapasha, A. M. Ukpong, and N. Chetty, Phys. Rev. B **85**, 125428 (2012).
[35] Y. Ding and Y. Wang, J. Phys. Chem. C **117**, 18266 (2013).
[36] J. Bardeen and W. Shockley, Phys. Rev. **80**, 72 (1950).
[37] J. Qiao, X. Kong, Z.-X. Hu, F. Yang, and W. Ji, Nat. Commun. **5**, 4475 (2014).
[38] Y. Cai, G. Zhang, and Y.-W. Zhang, J. Am. Chem. Soc. **136**, 6269 (2014).
[39] J. Dai and X. C. Zeng, Angew. Chem. Int. Ed. **54**, 7572 (2015).

[40] Y. Jing, Y. Ma, Y. Li, and T. Heine, Nano Lett. **17**, 1833 (2017).
[41] H. Lang, S. Zhang, and Z. Liu, Phys. Rev. B **94**, 235306 (2016).
[42] M. Cardona, Phys. Rev. **121**, 752 (1961).
[43] M. Cardona and H. S. Sommers, Phys. Rev. **122**, 1382 (1961).
[44] J. E. Rowe, F. H. Pollak, and M. Cardona, Phys. Rev. Lett. **22**, 933 (1969).
[45] F. Cerdeira, J. S. Dewitt, U. Rössler, and M. Cardona, Phys. Status Solidi B **41**, 735 (1970).
[46] L. D. Laude, F. H. Pollak, and M. Cardona, Phys. Rev. B **3**, 2623 (1971).
[47] S. Froyen and M. L. Cohen, Phys. Rev. B **28**, 3258 (1983).
[48] K. Chang, S. Froyen, and M. L. Cohen, Solid State Commun. **50**, 105 (1984).
[49] S. Fahy, K. J. Chang, S. G. Louie, and M. L. Cohen, Phys. Rev. B **35**, 5856 (1987).
[50] F. H. Pollak, in *Strained-Layer Superlattices: Physics*, edited by T. P. Pearsall, Semiconductors and Semimetals Vol. 32 (Elsevier, New York, 1990), pp. 17–53.
[51] F. H. Pollak and H. Qiang, Jpn. J. Appl. Phys. **32**, 101 (1993).
[52] X. Peng, Q. Wei, and A. Copple, Phys. Rev. B **90**, 085402 (2014).
[53] H. Zhang, Y. Ma, and Z. Chen, Nanoscale **7**, 19152 (2015).
[54] J. Zhou, Q. Wang, Q. Sun, and P. Jena, Nano Res. **9**, 1578 (2016).
[55] R. Fei, V. Tran, and L. Yang, Phys. Rev. B **91**, 195319 (2015).
[56] Q. Liu, X. Zhang, L. B. Abdalla, A. Fazzio, and A. Zunger, Nano Lett. **15**, 1222 (2015).
[57] K. Asano and C. Hotta, Phys. Rev. B **83**, 245125 (2011).
[58] See Supplemental Material at http://link.aps.org/supplemental/10.1103/PhysRevB.97.085418 for QE calculation and TB model details, symmetry breaking caused band gap opening, and Z_2 invariant and phonon calculations of c-BeP_2.
[59] P. L. de Andres, F. Guinea, and M. I. Katsnelson, Phys. Rev. B **86**, 245409 (2012).
[60] W. Bao, F. Miao, Z. Chen, H. Zhang, W. Jang, C. Dames, and C. N. Lau, Nat. Nanotechnol. **4**, 562 (2009).
[61] Z. F. Wang, Y. Zhang, and F. Liu, Phys. Rev. B **83**, 041403 (2011).
[62] N. W. Ashcroft, Phys. Rev. Lett. **92**, 187002 (2004).